



AFRL-RY-WP-TR-2013-0009

RADIO FREQUENCY AND OPTICAL METAMATERIALS

Dr. John S. Derov
Electro-Optics Components Branch
Aerospace Components & Subsystems Division

Alvin D. Drehman
Infrared Sensor Technology Branch
Electromagnetics Technology Division

Everett E. Crisman
University of Rhode Island

Beverly Turchinetz
Analog Technologies, Inc.

Teresa H. O'Donnell
Air Force Materiel Command
Electronic Systems Center

MARCH 2013
Final Report

Approved for public release; distribution unlimited.

See additional restrictions described on inside pages

STINFO COPY

AIR FORCE RESEARCH LABORATORY
SENSORS DIRECTORATE
WRIGHT-PATTERSON AIR FORCE BASE, OH 45433-7320
AIR FORCE MATERIEL COMMAND
UNITED STATES AIR FORCE

NOTICE AND SIGNATURE PAGE

Using Government drawings, specifications, or other data included in this document for any purpose other than Government procurement does not in any way obligate the U.S. Government. The fact that the Government formulated or supplied the drawings, specifications, or other data does not license the holder or any other person or corporation; or convey any rights or permission to manufacture, use, or sell any patented invention that may relate to them.

This report was cleared for public release by the USAF 88th Air Base Wing (88 ABW) Public Affairs Office (PAO) and is available to the general public, including foreign nationals.

Copies may be obtained from the Defense Technical Information Center (DTIC) (<http://www.dtic.mil>).

AFRL-RY-WP-TR-2013-0009 HAS BEEN REVIEWED AND IS APPROVED FOR PUBLICATION IN ACCORDANCE WITH THE ASSIGNED DISTRIBUTION STATEMENT.

*//signature//

JOHN S. DEROV, Work Unit Manager
Electro-Optics Components Branch
Aerospace Components & Subsystems
Division

//signature//

MARK G. SCHMITT, Chief
Electro-Optics Components Branch
Aerospace Components & Subsystems
Division

//signature//

BRADLEY D. CHRISTIANSEN, Lt. Col., USAF
Deputy Division Chief
Aerospace Components & Subsystems Division
Sensors Directorate

This report is published in the interest of scientific and technical information exchange, and its publication does not constitute the Government's approval or disapproval of its ideas or findings.

*Disseminated copies will show “//signature//” stamped or typed above the signature blocks.

REPORT DOCUMENTATION PAGE				Form Approved OMB No. 0704-0188	
<p>The public reporting burden for this collection of information is estimated to average 1 hour per response, including the time for reviewing instructions, searching existing data sources, gathering and maintaining the data needed, and completing and reviewing the collection of information. Send comments regarding this burden estimate or any other aspect of this collection of information, including suggestions for reducing this burden, to Department of Defense, Washington Headquarters Services, Directorate for Information Operations and Reports (0704-0188), 1215 Jefferson Davis Highway, Suite 1204, Arlington, VA 22202-4302. Respondents should be aware that notwithstanding any other provision of law, no person shall be subject to any penalty for failing to comply with a collection of information if it does not display a currently valid OMB control number. PLEASE DO NOT RETURN YOUR FORM TO THE ABOVE ADDRESS.</p>					
1. REPORT DATE (DD-MM-YY) March 2013		2. REPORT TYPE Final		3. DATES COVERED (From - To) 01 October 2009 – 01 September 2012	
4. TITLE AND SUBTITLE RADIO FREQUENCY AND OPTICAL METAMATERIALS				5a. CONTRACT NUMBER IN-HOUSE	
				5b. GRANT NUMBER	
				5c. PROGRAM ELEMENT NUMBER 61102F	
6. AUTHOR(S) Dr. John S. Derov (Aerospace Components & Subsystems Division, Electro-Optics Components Branch (AFRL/RYPD)) Alvin D. Drehman (Electromagnetics Technology Division, Infrared Sensor Technology Branch (AFRL/RYHI)) Everett E. Crisman (University of Rhode Island) Beverly Turchinetz (Analog Technologies, Inc.) Teresa H. O'Donnell (Air Force Materiel Command, Electronic Systems Center (AFMC/ESC))				5d. PROJECT NUMBER 2305	
				5e. TASK NUMBER HA	
				5f. WORK UNIT NUMBER Y05U	
7. PERFORMING ORGANIZATION NAME(S) AND ADDRESS(ES) Aerospace Components & Subsystems Division, Electro-Optics Components Branch (AFRL/RYPD) Sensors Directorate, Air Force Research Laboratory Wright-Patterson Air Force Base, OH 45433-7320 Air Force Materiel Command, United States Air Force				8. PERFORMING ORGANIZATION REPORT NUMBER AFRL-RY-WP-TR-2013-0009	
9. SPONSORING/MONITORING AGENCY NAME(S) AND ADDRESS(ES) Air Force Research Laboratory Sensors Directorate Wright-Patterson Air Force Base, OH 45433-7320 Air Force Materiel Command United States Air Force				10. SPONSORING/MONITORING AGENCY ACRONYM(S) AFRL/RYPD	
				11. SPONSORING/MONITORING AGENCY REPORT NUMBER(S) AFRL-RY-WP-TR-2013-0009	
12. DISTRIBUTION/AVAILABILITY STATEMENT Approved for public release; distribution unlimited.					
13. SUPPLEMENTARY NOTES PAO Case Number: 88ABW-11-6268, cleared 10 January 2013. Report contains color.					
14. ABSTRACT This research encompassed of study radio frequency (RF) and optical metamaterials. The RF study of metamaterials focuses on the polarization behavior of split-ring resonators (SRR) and wire-post (WP) elements and the spatially dispersive behavior of the SRR-WP elements. The optical study of metamaterials consisted of using the nanodot and nanoparticle media for their electric and magnetic plasmon behavior.					
15. SUBJECT TERMS negative refractive index, left-handed materials, double negative, metamaterials, plasmonics					
16. SECURITY CLASSIFICATION OF:			17. LIMITATION OF ABSTRACT: SAR	18. NUMBER OF PAGES 26	19a. NAME OF RESPONSIBLE PERSON (Monitor) John S. Derov 19b. TELEPHONE NUMBER (Include Area Code) N/A
a. REPORT Unclassified	b. ABSTRACT Unclassified	c. THIS PAGE Unclassified			

Table of Contents

Section	Page
List of Figures	ii
1.0 Summary	1
2.0 Methods, Assumptions, and Procedures	2
2.1 Radio Frequency Metamaterials	2
2.2 Surface Plasmons	7
2.3 Optical Metamaterial	10
3.0 References	19
List of Acronyms, Abbreviations, and Symbols	20

List of Figures

Figure	Page
Figure 1: Balanced Split-Ring Resonantors (SRRs).....	2
Figure 2: Measured Frequency Response and Refractive Index for SRR-WP Media.....	3
Figure 3: Frequency Response for Normalized Transmission of Unit Cell for SRR Gaps	3
Figure 4: Frequency Response for Normalized Transmission of SRR-WP Unit Cell.....	4
Figure 5: Comparison of Simulated and Measured Frequency Response for 0° and 90° SRRs	5
Figure 6: $\text{Re}(\mu)$ for Balanced SRR-WP at 0° and 90°	5
Figure 7: Frequency Response for $\text{Re}(\epsilon)$ and $\text{Re}(\mu)$	6
Figure 8: Frequency Response of ϵ and μ for SRR-WP Unit Cell	7
Figure 9: Surface Plasmon Wave at a Metal-Air Interface.....	8
Figure 10: Diagram of Prism-Spacer-Metal (Otto) Configuration	9
Figure 11: Gold Nanodots after Annealing.....	11
Figure 12: Transmittance for Nanodot Media	11
Figure 13: ATR Measurements as a Function of Incident Angle	12
Figure 14: Dispersion of Light in Free Space, Gold Film, and Cylindrical Prism	13
Figure 15: Multi-Layer Nanodot Medium Measured at Different Spacer Thicknesses	14
Figure 16: Dispersion for Gold Nanodot Media	14
Figure 17: Engheta Initial Design and Analysis	15
Figure 18: Permittivity and Permeability of the Nanosphere Ring.....	16
Figure 19: Diagram of the Four 90 nm Diameter Nanocylinders.....	16
Figure 20: Extracted Permittivity and Permeability of the Gold Nanocylinder Ring.....	17
Figure 21: Ebeam Patterned Nanoring made from the Nanocylinders	17
Figure 22: Simulated Results of the Patterned Nanorings	18

1.0 Summary

Radio frequency (RF) metamaterials were studied focusing on the polarization behavior of split-ring resonators (SRR) and wire-post (WP) elements and the spatially dispersive behavior of the SRR-WP elements. The SRR elements used in this study were two identical SRRs parallel to each other with their gaps in opposing orientations. The WP was placed between the rings with geometrical symmetry. The metal SRRs and WPs were separated by 10-mil thick dielectric with a relative permittivity of 2.2. The polarization behavior of the SRR-WP unit cell was simulated, by rotating SRRs in the unit cell between 0° and 170° about the center axis of the rings.

ANSYS's high frequency structure simulator (HFSS) was used to perform the simulation on the unit cell. The results showed how the rotation of the gap orientation relative to the incident linearly polarized electric field shifts the resonant frequency of the SRR-WP element.

The spatial behavior was studied by changing the SRR-WP unit cell's geometrical parameters such as the SRR diameter and WP post width. The simulated results showed the shift in resonant frequency and the change in effective permittivity and permeability with the variation of the SRRs geometrical parameters. By changing the geometrical parameters, coupling between neighboring SRRs and coupling between the WP and SRRs can be observed, thus affecting the relative permittivity and permeability of the metamaterial medium.

Optical metamaterials were also studied, which consisted of using the nanodot and nanoparticle media for their electric and magnetic plasmon behavior. A layered medium of random nanodots was fabricated and characterized for its plasmon behavior. No plasmon behavior was observed in the random nanodot medium, but polariton behavior was observed by probing the medium with transverse magnetic (TM) mode electromagnetic radiation. Ordered arrays of nanoparticles and nanoparticle clusters were also fabricated. The nanoparticle clusters consisted of four nanoparticles in the form of a ring and were fabricated to generate magnetic plasmon behavior in the medium. Simulations showed strong magnetic plasmon behavior in the 1.5- to 3- μm wavelength range with secondary weaker magnetic plasmon behavior in the 650- to 850-nm visible regime.

2.0 Methods, Assumptions, and Procedures

2.1 Radio Frequency Metamaterials

The RF research focused on balanced SRR and WP elements. The unit cells for the negative refractive index media [1] that were fabricated and characterized are shown in Figure 1. The unit cell consists of balanced SRRs [2] with the WP centered and between the SRRs. The balanced SRRs have 2 rings of the same diameter parallel to each other with their gaps oriented opposite as shown in Figure 1. When the SRRs are at resonance the current produced in each respective SRR is in the opposite direction, balancing the current distribution and generating a symmetric field around the SRRs. Figure 1 also shows the angular reference for orientation of the SRR gaps used throughout this study for the 0° and 90° orientation of the SRR gaps. This also defines a clockwise direction of rotation from 0° to 90° for the SRR gaps.

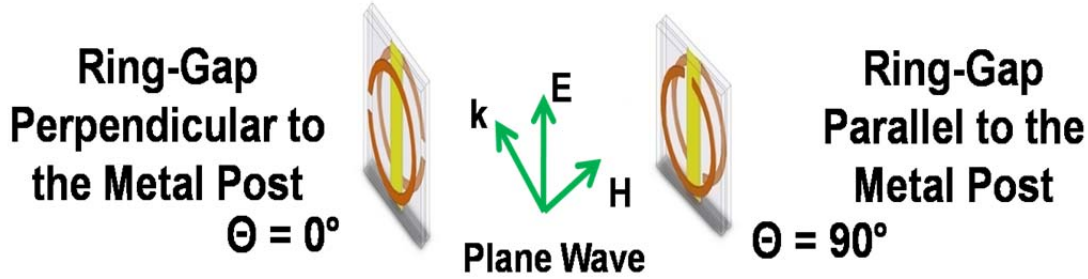
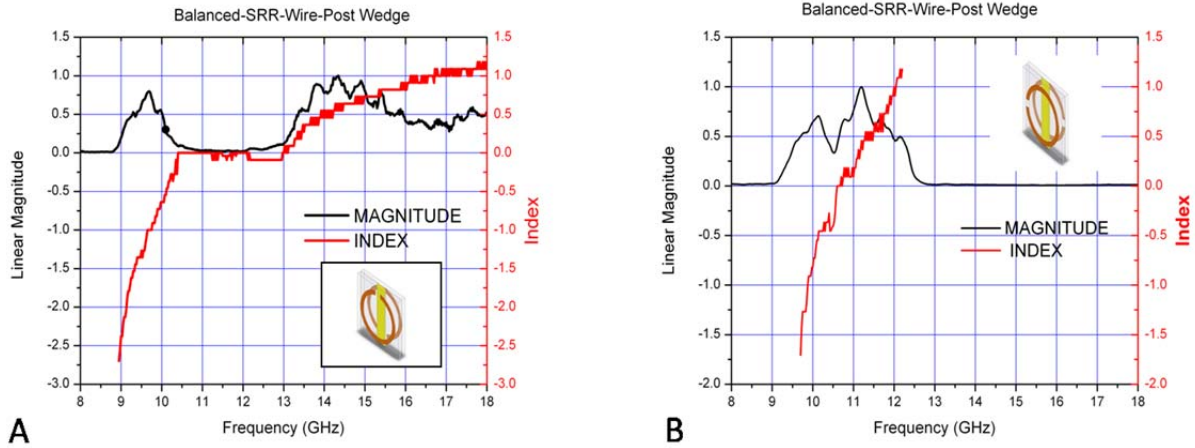


Figure 1: Balanced Split-Ring Resonators (SRRs)

Two SRRs of the same diameter parallel to each other with their gaps oriented opposite each other. The reference angles for 0° and 90° is also shown for the SRR gaps.

The measured frequency response and the refractive index as determined by Snell's law [3] are shown in Figure 2 for each of the configurations. Since the orientation of the electric field of the propagating wave is parallel to the WP as shown in Figure 1, it is the effect of the orientation of the electric field relative to the SRR gaps that is observed in the frequency response of the balanced SRR-WP media (Figure 2).



**Figure 2: Measured Frequency Response and Refractive Index for SRR-WP Media
In the two ring orientations (0° , 90°)**

Figure 3 shows that the frequency response of the SRRs is sensitive to the direction of the incident electric field relative to the gap of the SRRs. To investigate this further we ran simulations of the SRR-WP unit cell rotating the SRRs from 0° to 170° in 10° increments. In Figure 3 the frequency response of the normalized transmission is shown for gaps oriented at 10° and 170° . The results in Figure 3 show that the frequency response for the SRR gaps at 10° and 170° is almost identical and the rotation of the SRRs gap is symmetric about 90° .

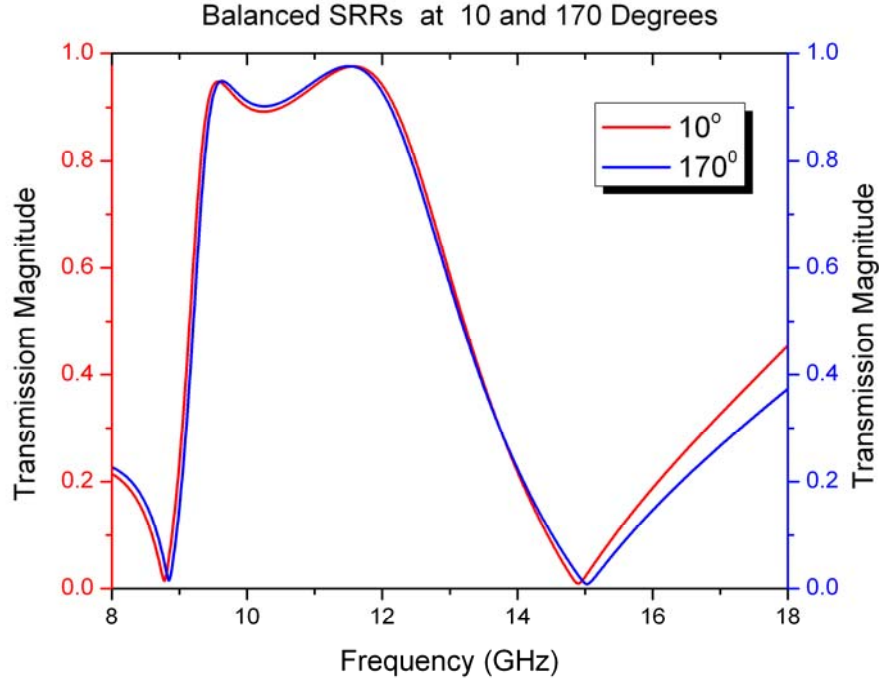


**Figure 3: Frequency Response for Normalized Transmission of Unit Cell for SRR Gaps
Oriented at 10° and 170° at symmetric orientations about 90°**

Figure 4 shows the results of the simulated frequency response of the normalized transmission through the unit cell at different gap angles 0° , 30° , 60° , and 90° . In Figure 4 it can be seen that the resonance for the unit cell moves from approximately 10 to 9 GHz, while the other resonance moves from approximately 12 to 15 GHz. The simulated frequency response of the unit cell at 0° and 90° is similar to the measured frequency response as shown in Figure 5.

Figure 4 also shows that the resonance of the SRRs is sensitive to the orientation of the SRRs gaps relative to the electric field of the incident wave. Thus, a linear polarized wave will respond differently in the medium depending on the orientation of the electric field of the incident wave to the gaps of the SRRs.

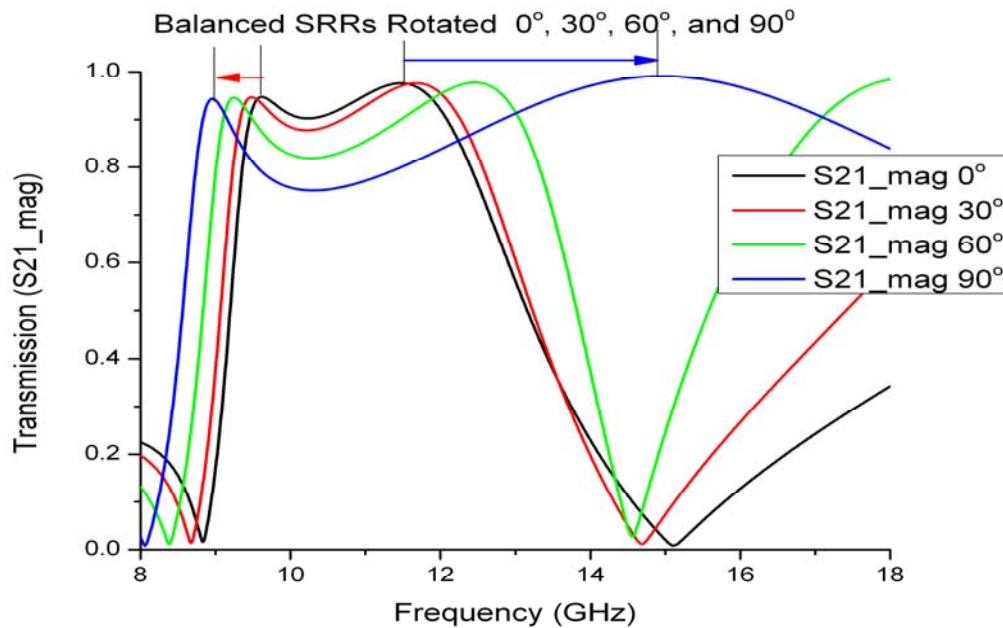


**Figure 4: Frequency Response for Normalized Transmission of SRR-WP Unit Cell
With the SRR gaps at 0° , 30° , 60° , and 90°**

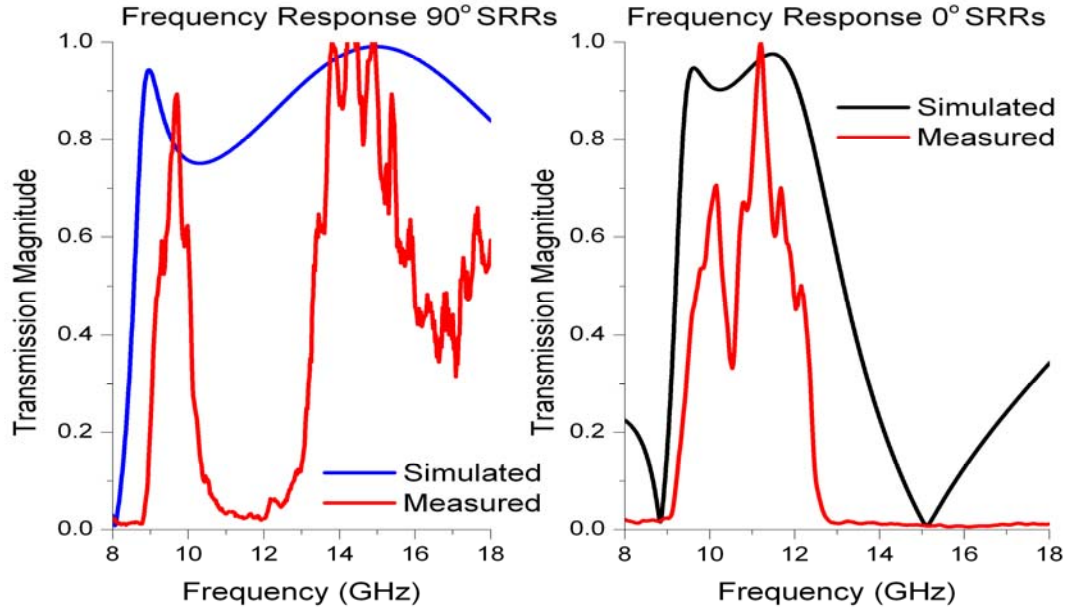


Figure 5: Comparison of Simulated and Measured Frequency Response for 0° and 90° SRRs

To understand what is going on in the media we need to look at how the permittivity (ϵ) and permeability (μ) is affected by the spatial change. The permeability for the unit cell with the SRR gaps at 0° and 90° is shown in Figure 6.

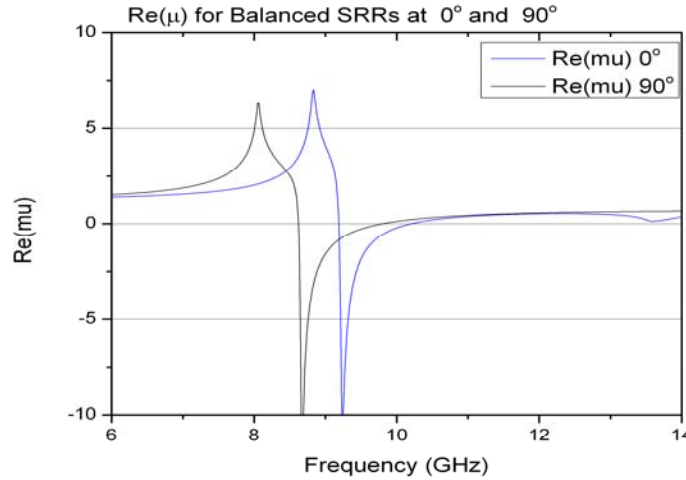


Figure 6: $\text{Re}(\mu)$ for Balanced SRR-WP at 0° and 90°

The non-Lorentzian line is most evident for μ between 6 and 8.5 GHz when the SRR gaps are at 90°

The line shape for the permeability is not as Lorentzian shaped as one would expect. As the gap of the SRR is rotated, the line shape of the μ approaches a Lorentzian shape. Since the line shape of μ shows the effect of changing the electric field orientation with respect to the SRR, we used the line shape of μ determined from the simulated scattering parameters of the unit cell to

determine the effect of the geometrical parameters of the SRRs and WPs.

We started by changing the diameter of the SRR in the unit cell. The outer diameter of the SRR was changed from 3.8 to 2.8 mm while holding the SRR gaps at 0° and the size of unit cell constant at 4.06 mm. Figure 6 shows the frequency response of the $\text{Re}(\mu)$ and $\text{Re}(\epsilon)$ for these conditions. As the outer diameter of the SRR changes from 3.8 to 2.8 mm the resonant frequency moves from lower to higher frequency. This is expected as the resonator line length goes from longer to shorter. It is the line shape of μ in Figure 7 that shows how the spatial dispersion is changing as the diameter of the SRRs is changed. As the diameter of the SRR is reduced in size, the line shape of μ is still asymmetric, but the line shape of μ is moving toward a Lorentzian line shape. The smallest SRR diameter at 2.8 mm unit cell is the least affected by the spatial dispersion.

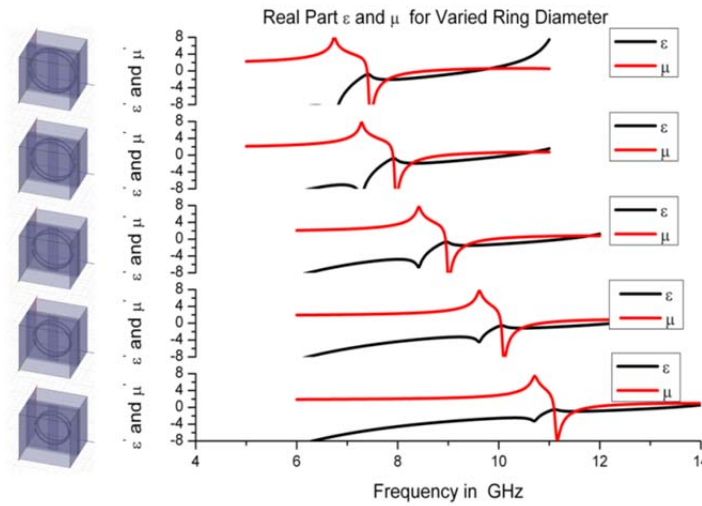


Figure 7: Frequency Response for $\text{Re}(\epsilon)$ and $\text{Re}(\mu)$
The diameter of the SRR was changed from 3.8 to 2.8 mm. The line shape of μ becomes more Lorentzian line like.

Since the line shape of μ was still asymmetric, the orientation of gaps and diameter of the SRR was held constant and the width of the WP was varied from 0.75 to 0.25 mm. Since the WP shape was varied, both ϵ and μ are affected. Figure 8 shows the frequency response of ϵ (blue and black lines) and μ (magenta and red lines). The line shape of μ becomes a symmetric Lorentzian shape at the resonant frequency when the width of the post is reduced to 0.25 mm.

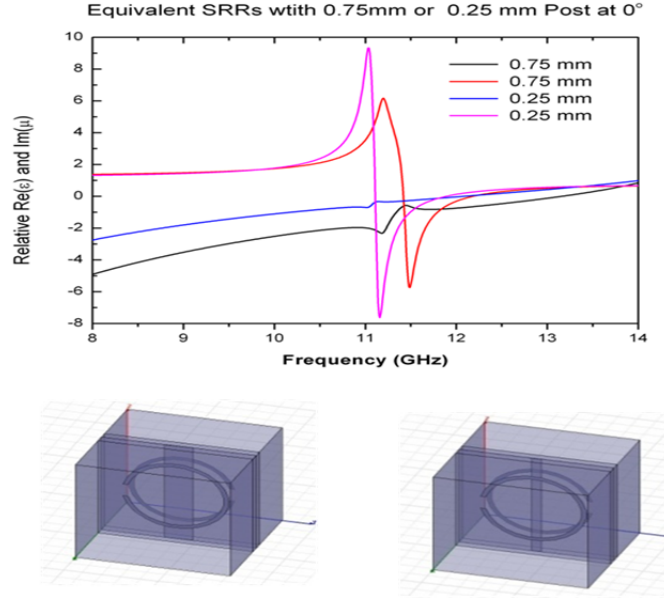


Figure 8: Frequency Response of ϵ and μ for SRR-WP Unit Cell
Diameter of the SRRs at 2.8 mm, the SRR gaps at 0° , and the size of the unit cell at 4.06 mm.
(The line shape for μ take on the expected Lorentzian line shape when the WP is 0.25mm wide)

Since the line shape of μ was affected by changing the width of the post, coupling between the WP and the SRRs is evident. The result indicates the coupling between neighboring SRRs and the SRRs and between the WP is important to produce a negative index of refraction.

2.2 Surface Plasmons

A plasmon is commonly defined as a collection of highly mobile electrons and ions that forms a neutral gas (e.g. the ionosphere). Metallic solids, with a high density of electrons, in their conduction bands or semiconductors with relatively high densities of carriers (electrons and holes) in both their valence and conduction bands can be modeled as a plasma under certain conditions. Plasmas not only exist in the volume of solids, but can also exist at the solid/ambient interfaces and the surface of the solid. The surface charge density forms small dipoles which can propagate a longitudinal wave which run along the surface and penetrate into a solid and into the adjacent atmosphere. The longitudinal waves are referred to as surface plasmon[4]. Recently surface plasmon interactions have been used to demonstrate optical devices such as sensors and readouts[5,6]. The properties of plasmons allow its wavelength to be much smaller than the free space wavelength at the same frequency. The smaller wavelength can enable optical components

below the Rayleigh limit of ordinary optical components. This could have ramifications in the size and speed of integrated optical components and devices.

The diagram in Figure 9 (a) shows the longitudinal surface plasmon wave propagating along a metal surface and the exponential decay of the surface wave in both media at the interface. Figure 9 (b) shows the dispersion for light and the surface plasmon in the metal. From the dispersion diagram it can be seen that the momentum of the surface plasmon k_{sp} and light k_0 is highly mismatched, indicating an ordinary light incident on the surface of the medium will not excite the surface plasmon.

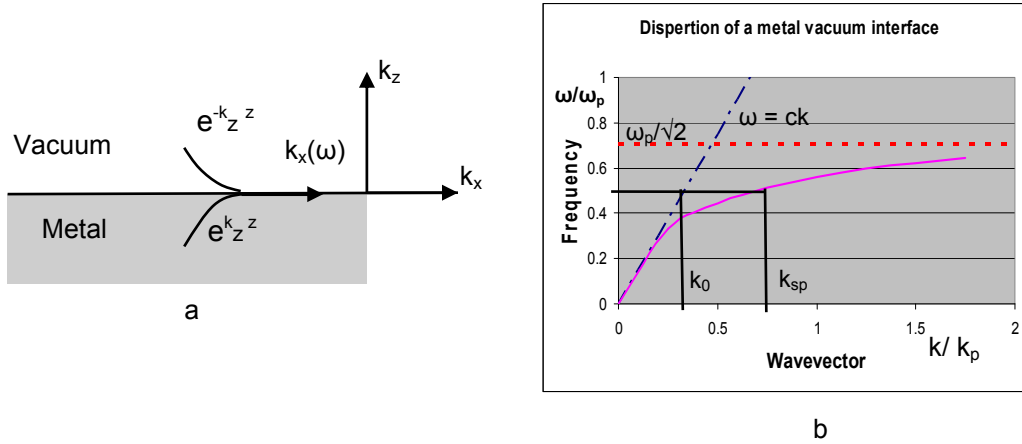


Figure 9: Surface Plasmon Wave at a Metal-Air Interface

(a) Diagrams the propagation of a surface Plasmon along an air-metal interface and illustrates the exponential decay of the wave for each medium at the interface. (b) Shows the dispersion for light in free space $\omega = ck$ and the dispersion of the surface plasmon at the air-metal interface asymptotically approaches the red dashed line is the frequency limit, $\omega_p/\sqrt{2}$, for the surface Plasmon

The prism coupler [7] shown in Figure 10 (a) is an attenuated-total-reflection (ATR) setup used to excite a surface plasmon resonance in the metal. Figure 10 (a) shows a prism-spacer-metal configuration. The prism is used to excite the surface plasmon resonance by total-internal-reflection at the prism-spacer interface. Total-internal-reflection is achieved when the refractive index of the spacer is less than the refractive index of the prism like a glass-air interface. Total-internal-reflection occurs when light incident at the prism-spacer interface is greater than or equal to a critical angle α . When total-internal-reflection occurs, an evanescent surface wave is produced at the prism-spacer (air) interface. The evanescent surface wave can then couple to the electric-dipole moments to drive the surface plasmon resonance. When the evanescent couples to the plasmon resonance the reflected light from prism is attenuated. The surface plasmon resonance generates a longitudinal propagating wave, the evanescent surface wave at the prism-air needs a longitudinal electric-field component. A transverse magnetic (TM) evanescent surface wave can be produced at the prism-air interface. The TM wave has a longitudinal electric-field component and is produced when linearly polarized light is parallel to the plane of incidence (p-polarized) at prism-air interface. When the evanescent TM wave couples to the plasmon resonance the intensity of the reflected light is attenuated.

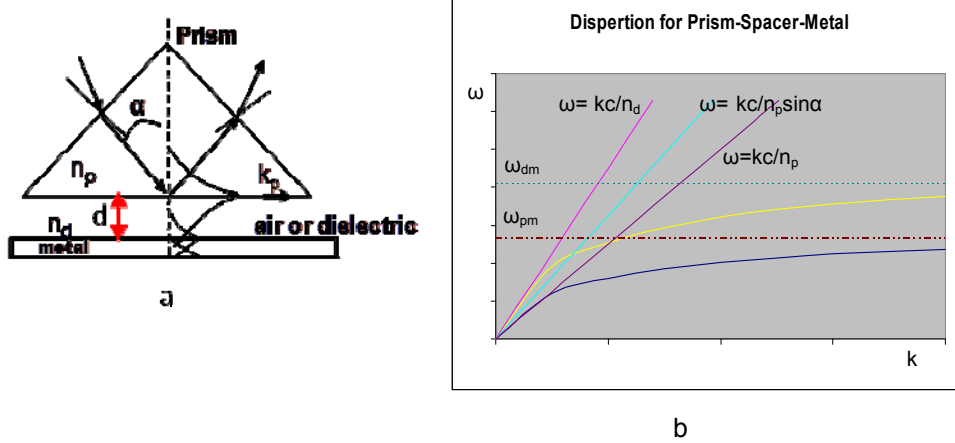


Figure 10: Diagram of Prism-Spacer-Metal (Otto) Configuration

(a) A diagram of a prism-spacer-metal configuration and (b) shows the dispersion relationships for light in free space $\omega = kc/n_d$ ($n_d=1$), light in the prism with a spacer layer $\omega = (kc/n_p)\sin\alpha$, light in an infinite medium with the same index as the prism $\omega = kc/n_p$, the surface plasmon dispersion for a metal-air interface (the line asymptotically approaching ω_{dm}), and surface plasmon dispersion for the metal-prism interface (the line asymptotically approaching ω_{pm}).

Figure 10 (b) shows the associated dispersion curves for light in air, light in the prism, an air-metal interface, and a prism-metal interface. The dispersion of the prism-metal asymptotically approaches $\frac{\omega_{pm}}{\sqrt{2}}$ where ω_{pm} is the plasma frequency for the prism-metal interface. The dispersion curve for light, in the prism is $\omega = \frac{kc}{n_p}$ where k is the wave vector, c is the speed of light in vacuum, and n_p is the refractive index of the prism. The light line for air in the plot is $\omega = \frac{kc}{n_d}$ where n_d is the refractive index for air and the dispersion curve for air-metal interface asymptotically approaches $\frac{\omega_{dm}}{\sqrt{2}}$ where ω_{dm} is the plasma frequency for the air-metal. In Figure 10 (b) it can be seen that the light line in the prism does not intersect the prism-metal dispersion curve nor does the light line for air intersect the air-metal dispersion curve. The dispersion relationship for the light line in prism-air-metal configuration is bound by the air-light line at the upper bound and prism-light line at the lower bound. The light line for the evanescent wave is given by $\omega = kc \sin \alpha / n_p$ where α is an angle equal to or greater than the critical angle for total internal reflection. In Figure 10 (b) the light-line for the evanescent wave intersects the plasmon dispersion curve for the air-metal interface. At this intersection point the momentum of the evanescent wave and the surface plasmon match driving the resonance of the surface plasmon. By changing the angle α , the light-line moves between the bounds of the light-lines for air and the prism. As α changes the light-line for the evanescent wave, it will intersect different points along the air-metal dispersion curve allowing the wave to couple with the plasmon resonance at those frequencies.

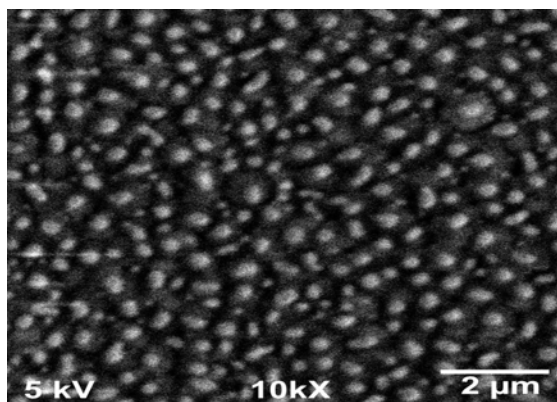
Since the plasmon resonance requires a longitudinal electric field to couple to its electric dipole moment, the plasmon interaction can be verified by changing the polarization of the light. A transverse electric (TE) evanescent surface wave can be produced at the prism-air interface. The TE wave has a longitudinal magnetic-field component. A TE wave is produced when polarized light is perpendicular to the plane of incidence (s-polarized) at the prism-air interface. The TE surface wave will not excite a surface plasmon resonance in the metal and therefore no attenuation will be evident in the reflected light.

2.3 Optical Metamaterial

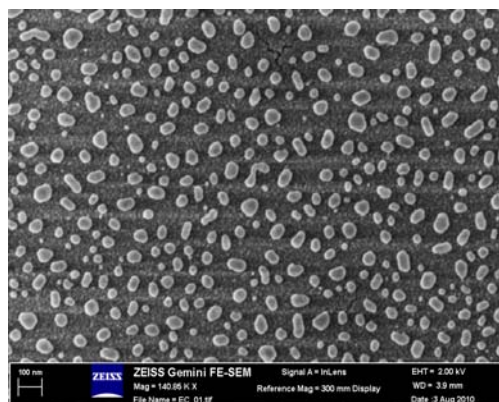
The initial demonstration of a negative refractive index metamaterial (NIM) came from Sir John Pendry's conceptual designs[8,9] for producing $\epsilon < 0$ and $\mu < 0$. Pendry's wire grid structure simulated behavior of a plasmon to produce an $\epsilon < 0$ and his SRRs simulated a ferromagnetic resonance behavior to produce $\mu < 0$ at microwave frequencies.

Since plasmons exist at optical frequencies, the problem is finding a structure at optical frequencies to produce $\mu < 0$ like the SRRs since SRRs do not scale to optical frequencies. NIM media at optical frequencies will provide the material for fabricating optical and or electro-optical components and devices that do not presently exist, but are wanted for applications like electronic beam steering at optical frequencies. Nano-size particles like dots, spheres, rods, etc... have been proposed in the literature[10]. NIM material composites use nano-size conductors in a dielectric or semiconductor medium. The problem with validating the proposed nano-structure and making an optical NIM is controlling the size and placement of the nanoparticles during fabrication. One of the simplest nano-size particles are dots. The nanodots can produce resonant electric and magnetic dipole moments to generate a negative ϵ and μ .

Characterization of the nanodots electromagnetic properties in single- and multi- layer media allow us to determine plasmon and NIM behavior. We have constructed nanodot media by means of random size and oriented gold colloidal dots layered between aluminum oxide films. These dots were made by depositing a gold film of a defined thickness on the sputtered layer of aluminum oxide. The thickness of the gold film allowed control of the average diameter of the dot. The gold film was then annealed between 500°C and 600°C causing the gold to coagulate into dots. Another layer of aluminum oxide was then deposited over the nanodots and the gold processing was repeated. Up to four layers of nanodots/alumina have been made this way, which produced nanodots that had between 500 nm and 70 nm for the given medium. Figure 11 shows nanodots formed after the annealing process. The nanodots shown in Figure 11(a) are the 500 nm dot medium and Figure 11(b) shows the 70 nm dot medium after the annealing process.



(a)

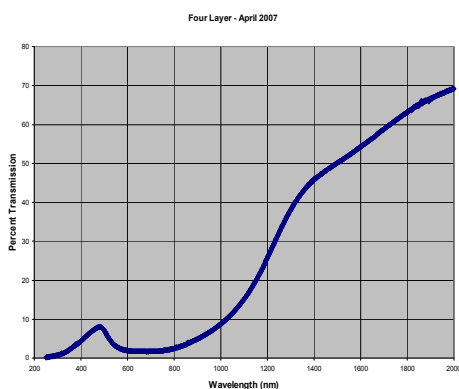


(b)

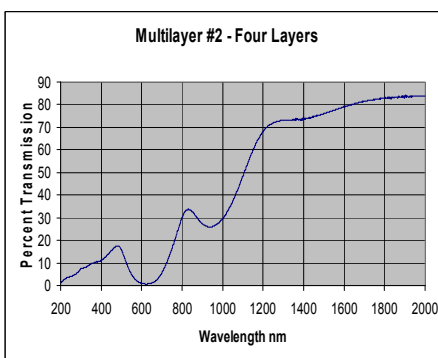
Figure 11: Gold Nanodots after Annealing

Both images were taken at 10,000X and have a 2 micrometer reference line. (a) SEM 500nm dot medium, (b) FE-SEM of 70nm dot medium

The transmittance of the 500nm dot and 70nm dot medium was measured from 200 to 2000nm and are shown in Figure 12. The transmittance 500nm dot medium is shown in Figure 12(a). The transmittance shows light is being absorbed between 500 and 800 nm and the transmittance is $> 60\%$ in the 1500nm. The transmittance for the 70nm dot medium in Figure 12(b) shows the absorption at approximately 600 nm and $> 70\%$ transmittance at 1200 nm. This has been observed in gold nanoparticle and reported in the literature. The absorption was referred to as an anomalous absorption band[11].



(a)



(b)

Figure 12: Transmittance for Nanodot Media

(a) Transmittance response for the 500nm nanodot medium, (b) the transmittance response for the 70nm nanodot medium

The ATR technique described in Section 3 was used to characterize the random nanodot media. We started the characterization process by characterizing the plasmon behavior of a gold film to provide a baseline for our ATR measurements. The intensity of the reflectivity was measured as a function of angle for the light incident at the air-prism interface. Figure 13 shows results for the continuous gold metal film from the ATR measurements. The measurements show that a surface

plasmon resonance occurs for the p-polarized TM wave above the critical angle, but no resonance is observed for the s-polarized TE wave. The coupling efficiency of the TM wave to the plasmon resonance can be controlled by adjusting the thickness of the air gap. In Figure 13 the dip in the reflectivity for the p-polarized curves above the critical angle indicates a surface plasmon resonance in the gold film. Using the angle of incidence, at which the plasmon resonance occurs, the wave vector for the surface plasmon wave at the metal surface can be determined. The thickness of the air-gap, shown in Figure 10a, was also changed in the measurement. The depth of the dip for the resonance increases as the air-gap thickness decreases, indicating higher coupling efficiency to the surface plasmon resonance and from the width of the dip, the loss for the surface plasmon wave can be determined.

A complex wave vector given by $k = k_r + k_i$ can be used to determine the propagating wave vector and attenuation of the plasmon wave across the surface of the gold film. The propagating wave vector is given by the real part $k_r = k_0 n_p \sin(\alpha)$ where k_0 is the free space wavelength, n_p is the refractive index of the prism, and α is the minimum angle of the absorption dip. The imaginary part of $k_i = k_0 n_p \cos(\alpha) \Delta\alpha$ where $\Delta\alpha$ is the difference in angle at the halfwidth of the absorption dip. The imaginary part $k_i = k_{im} + k_{irad} e^{-2\Delta k d}$ where k_{im} is the energy absorbed in the metal and k_{irad} is the radiation damping due to the emission of the light back into the prism. The radiation damping is also dependent on the thickness of the spacer layer 'd' shown in Figure 10 between the film and the prism and $\Delta k = \sqrt{(k_r^2 - k_0^2)}$.

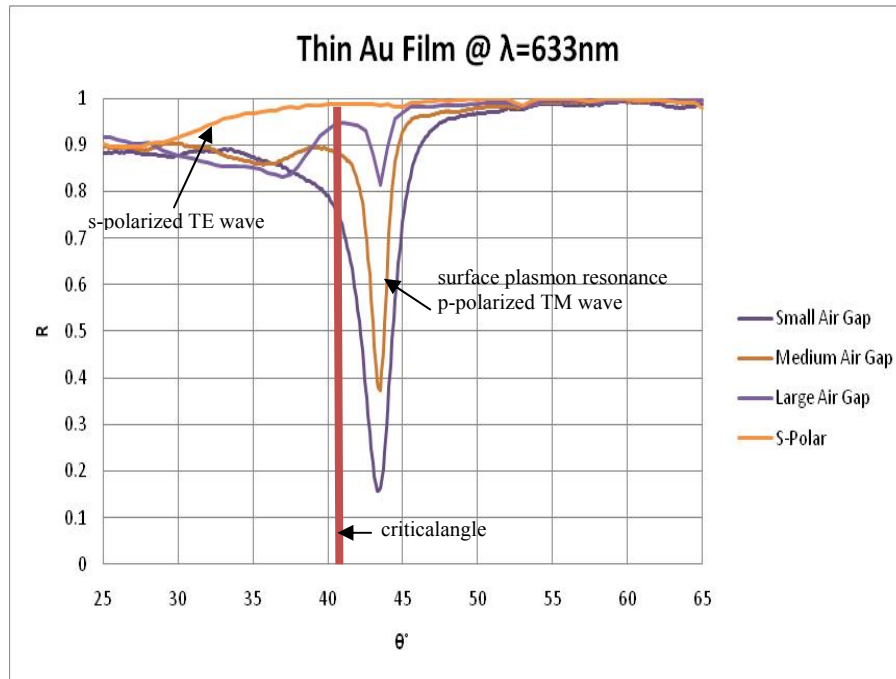


Figure 13: ATR Measurements as a Function of Incident Angle
A surface plasmon resonance is observed for p-polarized light above the critical angle and no resonance occurs for the s-polarized light

The results of the ATR measurements were used to determine the dispersion relation for the continuous gold metal film. The dispersion for the film is shown in Figure 14. The dispersion for the plasmon resonance of the gold film is shown bound by the dispersion of light in free space and the dispersion of the light in the prism, as discussed in Section 3.

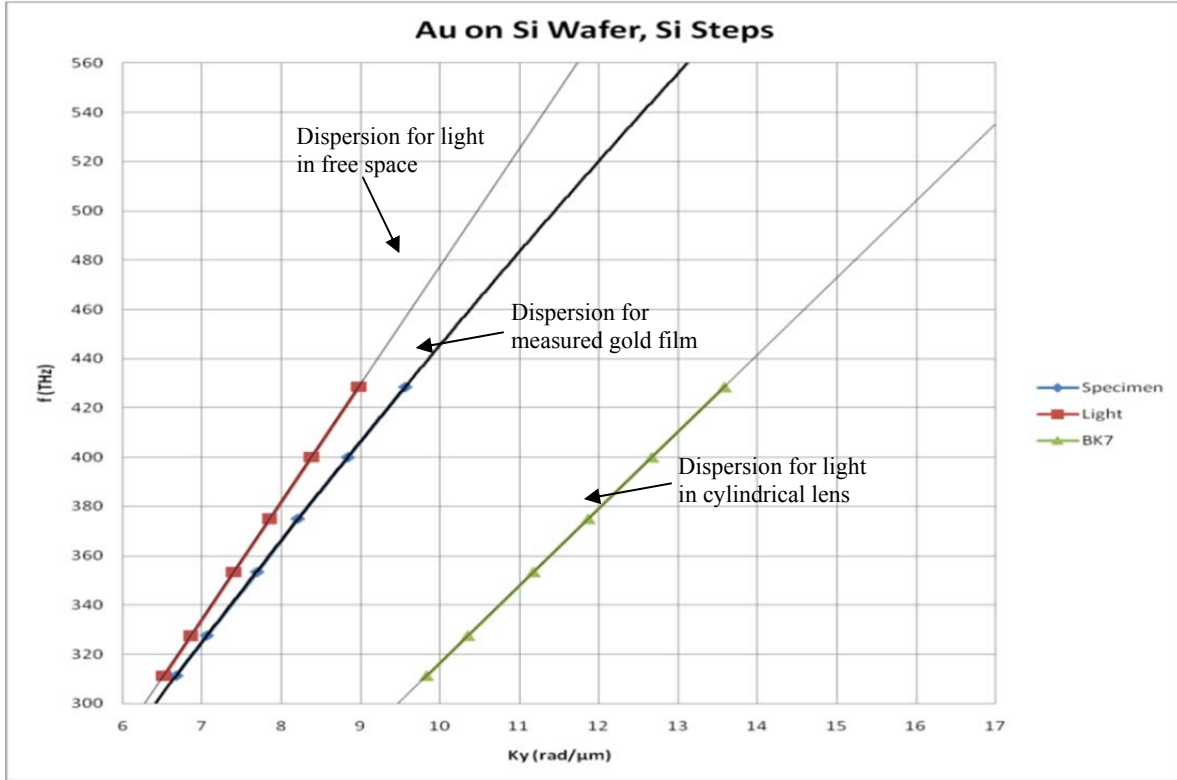


Figure 14: Dispersion of Light in Free Space, Gold Film, and Cylindrical Prism
*The dispersion for light in free space is $\omega = c*k$, for light in the gold film is $\omega = (c*k/(n*sina))$, and for light in the cylindrical lens is $\omega=c*k/(n)$*

A 4-layer nanodot medium was characterized using the above ATR technique. The results of the measurements are shown in Figure 15. Absorption of the light is observed above the critical angle. The absorption depth of the dip for the nanodot medium increased as the air-gap thickness decreased similar to the gold film. The observed absorption dip for the multi-layer nanodot is broader than the dips for the gold film. An explanation for the broadened absorption dip is the size distribution of the nanodots in the medium since the medium is made up of different size nanodots, as shown in Figure 10(b). The size of the nanodots determines the resonant wavelength for the nanodot. The wavelength exciting the resonance is the wavelength of the evanescent wave, which is dependent on the incident angle of the light at the air prism interface. Since the nanodot size varies, the wavelength of the evanescent can excite the resonance of the different size nanodots broadening the dip.

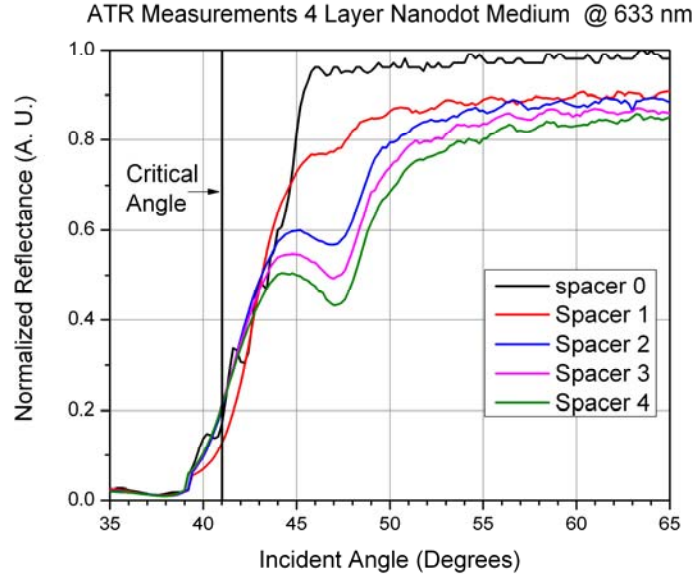
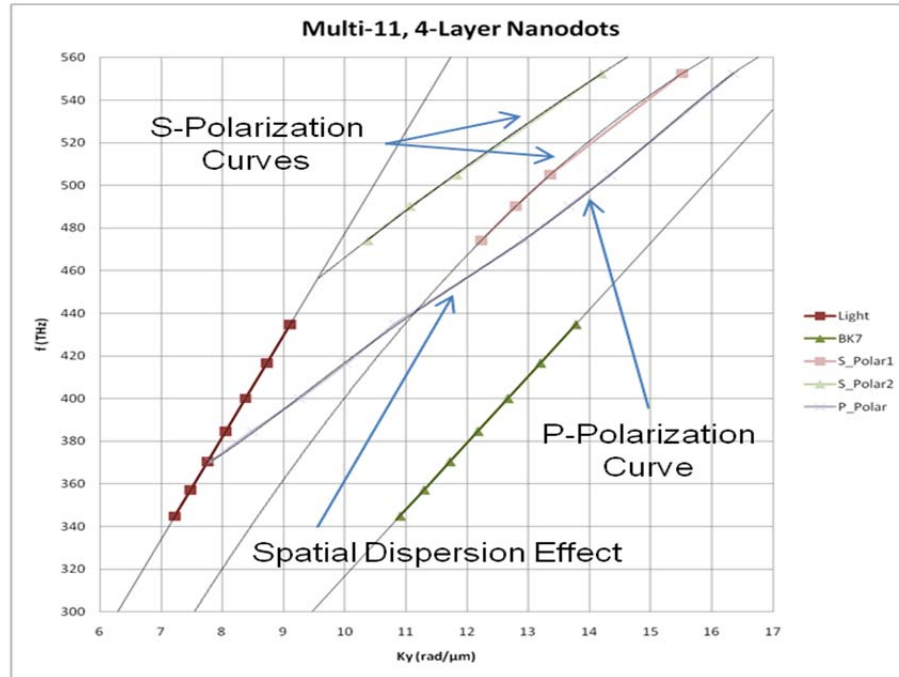


Figure 15: Multi-Layer Nanodot Medium Measured at Different Spacer Thicknesses

The dispersion for the 4-layer nanodot medium was also determined using the ATR measurements. The dispersion for the 4-layer nanodot medium is shown in Figure 16.



**Figure 16: Dispersion for Gold Nanodot Media
*S- and P-polarization, Cylindrical Lens, and Polariton Behavior***

The dispersion for the nanodot medium is bound by light in free space and by light in the cylindrical-lens as well. The results in Figure 16 show that the nanodot medium responds to both

p- and s- polarization. The dispersion for the p- polarization response has an inflection point at approximately 445 THz. The line shape of the p-polarized dispersion curve indicates that there is a plasmon-polariton [12] response at wavelengths below 445 THz and above 445 THz no plasmon response is observed. The inflection point at 445 THz is marked as the spatial dispersion effect in the p-polarized Figure 16. There is no band gap in the nanodot medium due to spatial dispersion like the band gap that occurs for the plasmon behavior of the gold film.

For magnetic plasmon behavior in a medium, a nanodot inclusion like the one shown in Figure 17 was chosen. The nanodot structure consisted of 4 silver nanospheres arranged in a ring. The nanosphere ring is analogous to split-ring resonators (SRRs) at RF frequencies. The cluster of nanoparticles forming a ring was proposed by Professors Engheta and Alù [13]. Figure 17 shows simulated results of the silver 4-nanoparticle ring obtained from Prof. Engheta. For the simulation, the four silver nanoparticles were suspended in air and results show the nanoparticle ring resonating at 560THz. Since the nanoring in Figure 17 was modeled as four silver nanospheres suspended in air, this nanoring could not be fabricated. The fabrication processes available to us for patterning the nanorings are Ebeam or nanosphere lithography.

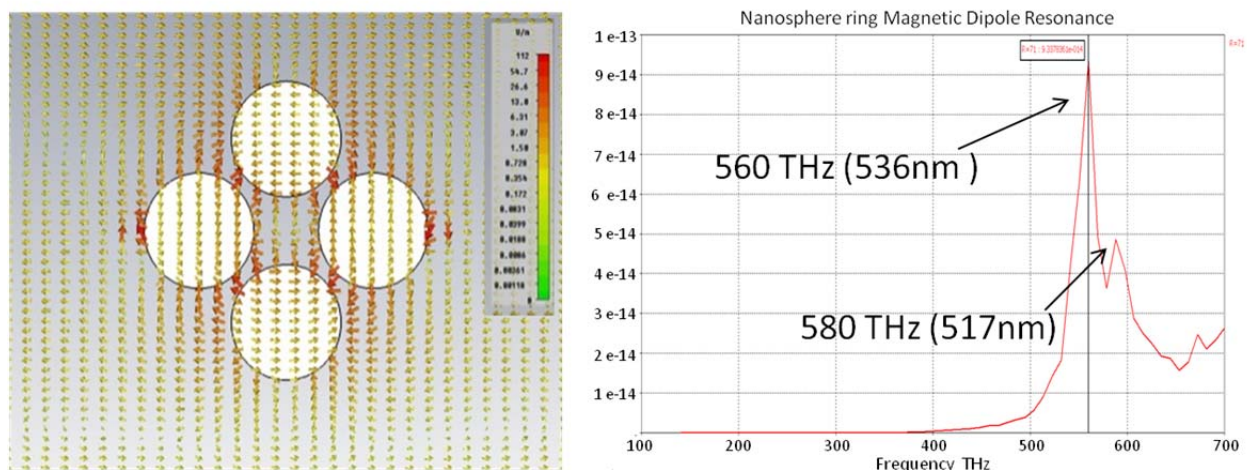
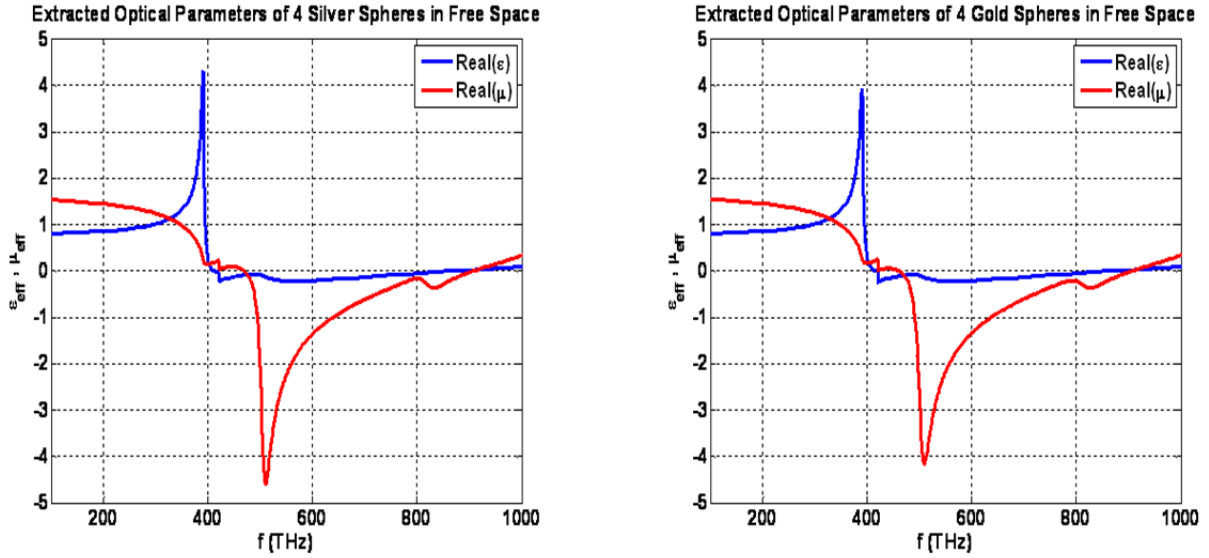


Figure 17: Engheta Initial Design and Analysis
Left is a 4-element nanosphere ring (4NSR) and analysis of H-Field between spheres. Right is H-Field vs. Frequency.

These lithographic processes are planar and require the pattern to be printed on a substrate. This limits the shape of the nanoparticles to cylinders for the Ebeam and a pyramidal shape particle for the nanosphere lithography. The use of the substrate and the change in the shape of the nanoparticles means our nanorings will not behave like the modeled silver nanoparticle ring suspended in air. To confirm the HFSS simulation results of our nanoparticle would agree with Engheta and Alù's Comsol simulation. We started with Engheta and Alù's 4- sphere nanoring suspended in air and simulated it in HFSS. We modeled the Engheta and Alù's nanoring with silver and gold since we planned to use gold for the initial study. The results from the HFSS simulation are shown below in Figure 18.



**Figure 18: Permittivity and Permeability of the Nanosphere Ring
Made of (Left) Silver, (Right) Gold**

Figure 18 shows the real part of ϵ and μ for the 4 nanospherering suspended in air for silver and gold as a function of frequency. The real part of μ shows a strong resonance with a negative value at approximately 520 THz, very close to Engheta and Alu's 560THz peak magnetic field resonance. It also shows it is negative from approximately 500 to 800 THz, which includes the 500-700THz range at which strong magnetic fields are observed in Engheta and Alu's model. Since results of our HFSS simulation matched those of Engheta and Alu, we modeled our 4 nanocylinder ring suspended in air and on an aluminum oxide substrate in HFSS. A diagram for the nanoring used in the simulation is shown in Figure 19. The diagram shows four nanocylinders centered around a 130 nm circle. This leaves the spacing between the nanocylinders at 2 nm.

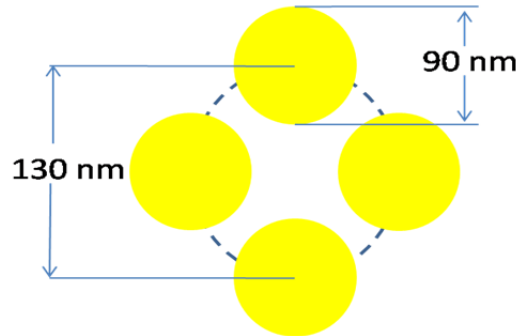


**Figure 19: Diagram of the Four 90 nm Diameter Nanocylinders
Centered on a 130 nm circle to form the ring used for the HFSS simulations and for the
patterned Ebeam lithography**

The simulated results for the gold nanoring with cylindrical particles suspended in air and on an aluminum oxide substrate are shown in Figure 20.

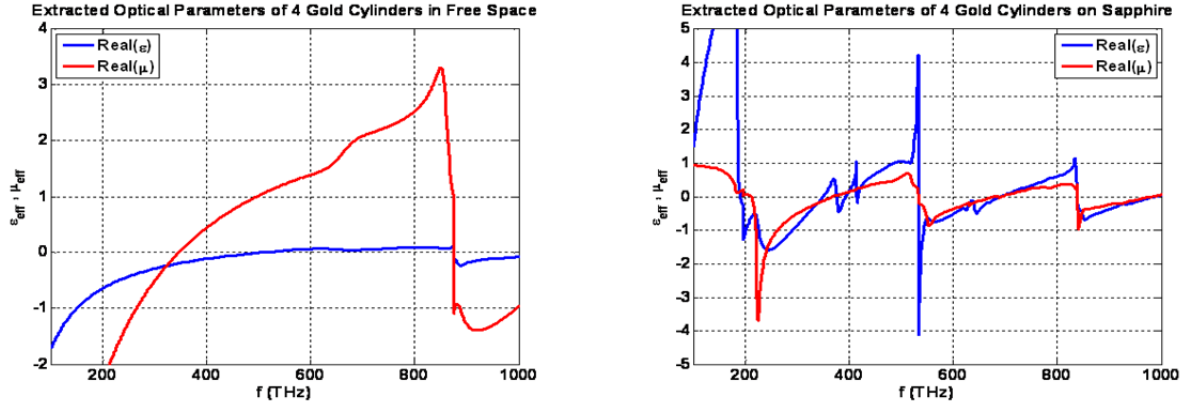


Figure 20: Extracted Permittivity and Permeability of the Gold Nanocylinder Ring
In air (Left), and on a sapphire substrate (Right)

The frequency response of the real part of μ for the nanocylinder ring suspended in air shown on the left in Figure 20 is significantly different from the nanosphere ring suspended in air. The resonance in μ for the nanoring with the cylinders suspended in air is about 860THz, which is above the resonant frequency of μ for the nanoring with spheres suspended in air (~520THz). The nanocylinder ring on the aluminum oxide substrate shown on the right of Figure 20 has more structure than the nanocylinder ring suspended in air. The nanocylinder ring on aluminum oxide has 3 distinct resonances at approximately 250, 550, and 850THz. Ebeam lithography was used to fabricate an array of nanocylinder rings on an aluminum oxide substrate. The fabricated nanorings are shown in Figure 21. Though Ebeam lithography is precise, the critical dimensions for the nanocylinders are beyond the resolution of the Ebeam lithography system. In Figure 21 one can see the imperfections of the nanorings for various fabricated nanocylinder and ring diameters. The imperfections will affect the behavior of the nanorings.

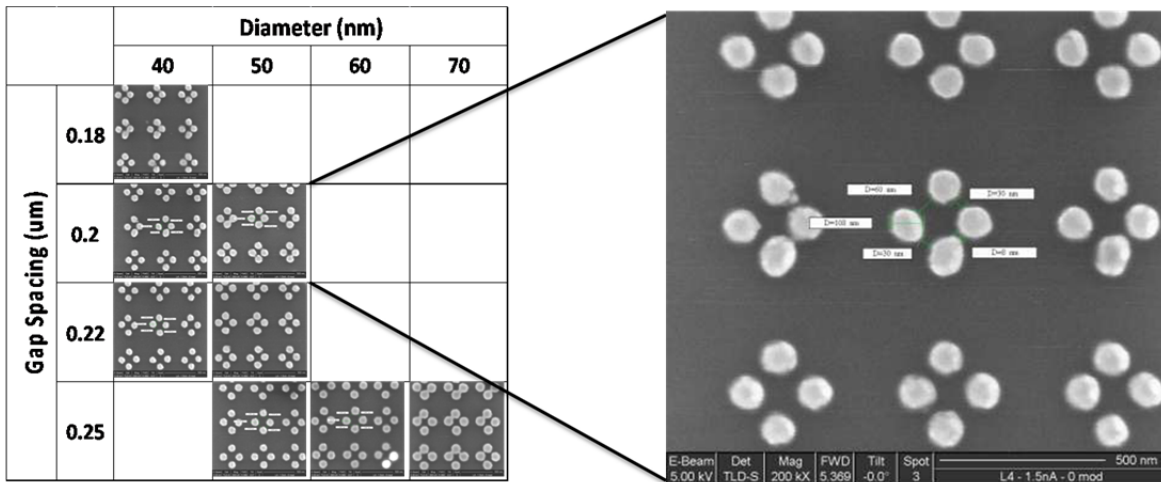


Figure 21: Ebeam Patterned Nanoring made from the Nanocylinders
The nanocylinders are required to be 90 nm in diameter with a 2-nm spacing between the cylinders in the ring as shown in Figure 19

Figure 21 on the right shows a case where all nanocylinders are resolved but with some variation in the diameter and spacing. To determine the effects of cylinder size and spacing variations of

the nanorings, an average value for the cylinder size and spacing was used to simulate the nanoring. The result of the simulation is shown in Figure 22.

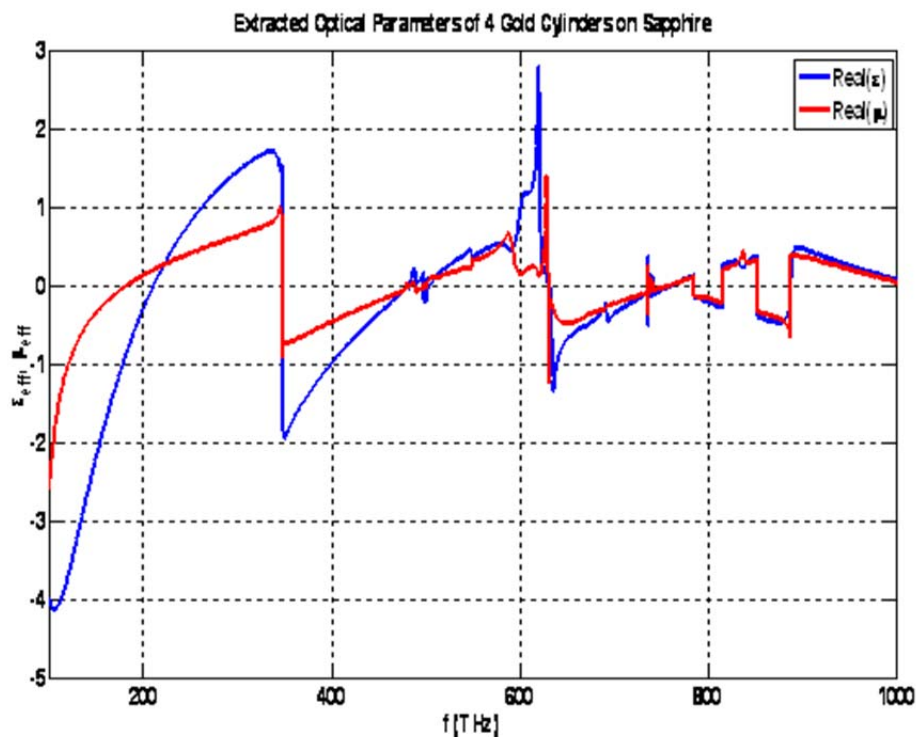


Figure 22: Simulated Results of the Patterned Nanorings
Using mean values for the cylinder diameters and spacing

The simulation results shown in Figure 22 show that the first two resonances for the nanocylinder ring have moved down in frequency compared to resonances in Figure 20, as expected since the diameter and spacing has increased. The changes in the resonances observed in Figures 20 and 22 indicate that controlling the diameter and spacing of the nanocylinders in the fabrication process is critical for building optical metamaterials at the desired wavelengths.

We are presently characterizing the nanocylinder rings to determine the resonant frequency of the fabricated 4 nanocylinder rings and to determine how the size and spacing of the nanocylinders in the ring affect its predicted response compared to its actual response. A series of SRR-WP media are being fabricated to validate the effect of the neighbor to neighbor coupling of the SRR-WP unit cells and the effect of coupling between SRRs and WP.

3.0 References

1. Veselago V. G., "The Electrodynamics of Substances with Simultaneously Negative Values of ϵ and μ ," Soviet Physics USPEKHI, Vol. 10, No. 4, Jan-Feb 1968
2. Marqués R., Martel J., Mesa F., and Medina F., "Left-Handed-Media Simulation and Transmission of EM Wave in Subwavelength Split-Ring-Resonator-Loaded Metallic Waveguides," Phys. Rev. Lett., Vol. 89, No. 18, 28 Oct. 2002
3. Derov J. S., Turchinets B. W., Crisman E. E., Drehamn A. J., and Wing R. M., "Free Space Measurements of Negative Refraction With Varying Angles of Incidence," IEEE Microwave and Wireless Components Lett., Vol. 15 No. 9 Sept. 2005
4. H. Raether, "Excitation of Plasmons and Interband Transition by Electrons", Springer-Verlag, 1980, Chap. 10
5. Stefan A. Maier and Harry A. Atwater, "Plasmonics: Localization and guiding of electromagnetic energy in metal/dielectric structure", J. Appl. Phys., 98, 01101, 2005
6. Harry A Atwater, "The Promise of Plasmonics", Scientific American, pp. 56-63, April, 2007
7. Otto A., Excitation of Nonradiative Surface Plasma Waves in Silver by the Frustrated Total Reflection," Zeitschrift für Physik 216, pp.398-410 , 1968
8. D. R. Smith, Willie J. Padilla, D. C. Vier, S. C. Nemat-Nasser, and S. Schultz, "Composite Medium with Simultaneously Negative Permeability and Permittivity", Phys. Rev. Lett., Vol. 84, No. 18, May 2000, pp 4184-418
9. R. A. Shelby, D. R. Smith, and S. Schultz, "Experimental verification of negative index of refraction," Science, Vol. 292, pp. 77-79, 2001
10. Andrea Alu and Nader Engheta, "Guided Modes in a Waveguide Filled With a Pair of Single-Negative (SNG), Double-Negative (DNG) and/or Double-Positive (DSP) Layers", IEEE Trans. MTT., Vol. 52, No. 1, pp. 199-206, Jan. 2004
11. Granqvist C.G., and Hunderi o., "Optical Properties of Ultrafine Gold Particles," Phys. Rev. B, Vol. 16, No. 18, 15 Oct. 1977, pp 3515-3534
12. "Polaritons," Proceeding of the First Taormina Conference on the Structure of Matter, Taormina, Italy, 1972, ISBN 0-08-017825-1
13. Alù A., Salandrino A., and Engheta N., "Negative Effective permeability and Left-Handed Materials at Optical Frequency," Opt. Express Vol. 14, No. 4 pp. 1557-1567, 20 Feb. 2006

List of Acronyms, Abbreviations, and Symbols

Acronym	Description
Al ₂ O ₃	Aluminum Oxide
ATR	Attenuated Total Reflection
GHz	Giga-Hertz
HFSS	High Frequency Structure Simulator
NIM	Negative refractive Index Metamaterial
RF	Radio Frequency
SRR	Split-Ring-Resonator
TE	Transverse Electric
THz	Terra-Hertz
TM	Transverse Magnetic
WP	Wire Post